



Modelling gas motion in a rapid-compression machine

M.G. MEERE¹, B. GLEESON¹ and J.M. SIMMIE²

Department of Mathematical Physics, NUI, Galway, Ireland

²Department of Chemistry, NUI, Galway, Ireland

Received 25 July 2001; accepted in revised form 8 May 2002

Abstract. In this paper, a model which describes the behaviour of the pressure, density and temperature of a gas mixture in a rapid compression machine is developed and analyzed. The model consists of a coupled system of nonlinear partial differential equations, and both formal asymptotic and numerical solutions are presented. Using asymptotic techniques, a simple discrete algorithm which tracks the time evolution of the pressure, temperature and density of the gas in the chamber core is derived. The results which this algorithm predict are in good agreement with experimental data.

Key words: gasdynamics, rapid-compression machines, shock-waves, singular perturbation theory

1. Introduction

1.1. RAPID-COMPRESSSION MACHINES

A rapid-compression machine is a device used to study the auto-ignition of gas mixtures at high pressures and temperatures, with particular reference to auto-ignition in internal combustion engines; see [1–3]. A typical combustion engine is a very dirty and complex environment, and this has prompted the development of rapid-compression machines which enable the scientific study of compression and ignition in engines in a cleaner and simpler setting. In Figure 1 we schematically illustrate a two-piston rapid-compression machine, such as the one in the department of Chemistry at NUI, Galway. However, single-piston machines, with a piston at one end and a stationary solid wall at the other, are more typical. The analysis developed in this paper is appropriate to both single- and two-piston machines.

The operation of a rapid-compression machine is very simple - the pistons are simultaneously driven in pneumatically, compressing the enclosed gas mixture, thereby causing the gas pressure, temperature and density to rise quickly. In Figures 1(a), 1(b) and 1(c) we schematically represent a rapid-compression machine prior to, during, and after compression, respectively. The ratio of the final volume to the initial volume of the compression chamber for the machine at NUI, Galway is about 1:12, this value being typical of other machines. At the end of the compression, the gas mixture will typically have been pushed into a pressure and temperature regime where auto-ignition can occur.

In Figure 2, we display an experimental pressure profile for a $H_2/O_2/N_2/Ar$ mixture which has been taken from Brett *et al.* [4], with the kind permission of the authors. In this graph, the time $t = 0$ corresponds to the end of the compression time. We note that, for the greater part of the compression, the pressure in the chamber is rising quite gently, but that towards the end of the compression (that is, just before $t = 0$), there is a steep rise in the pressure. After compression, the pressure profile levels off as expected; the extremely steep rise at the end of

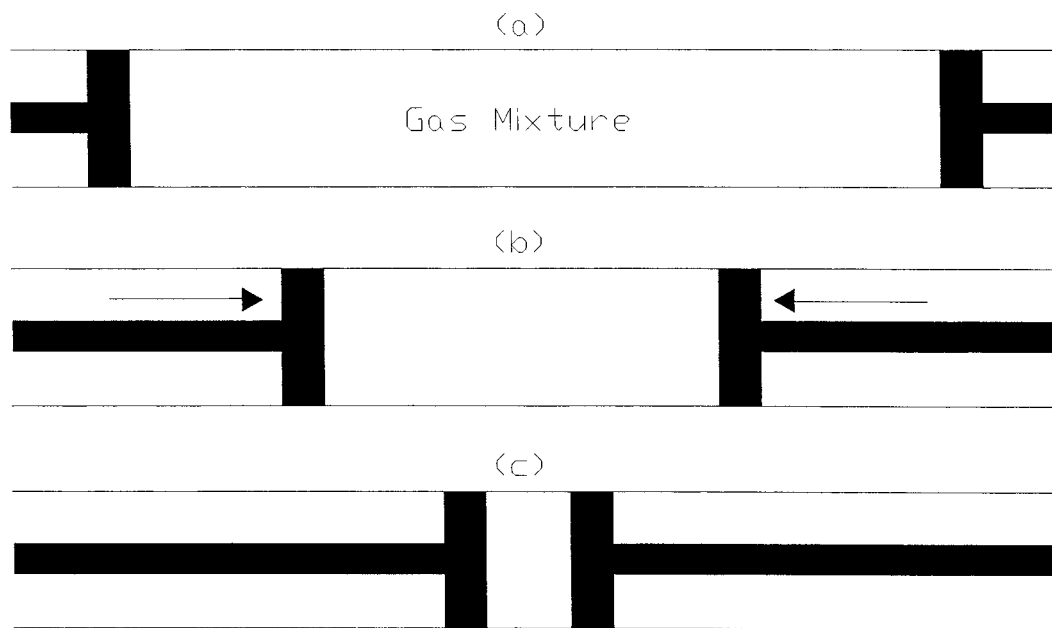


Figure 1. Schematic illustrating the operation of a rapid-compression machine; we have shown the configuration (a) prior to compression, (b) during compression and (c) after compression.

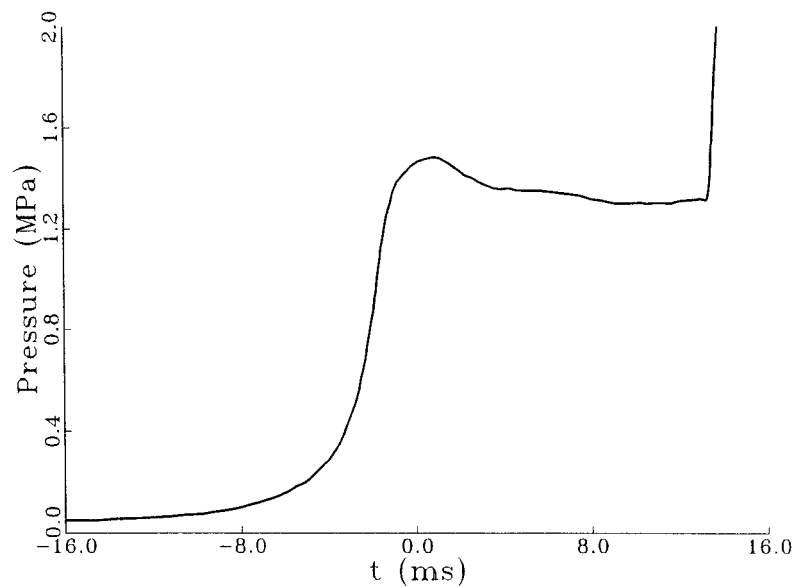


Figure 2. An experimental pressure profile for a gas mixture $\text{H}_2/\text{O}_2/\text{N}_2/\text{Ar} = 2/1/2/3$, as measured in the rapid-compression machine at NUI, Galway. It is taken from [4], and has an initial pressure of 0.05 MPa and an initial temperature of 344 K.

the profile corresponds to the ignition of the mixture. We note that the compression time and the time delay to ignition after compression are both $O(10)$ ms.

The pressure history is the only quantity which is measured in experiments. However, the temperature in the core after compression is the quantity which is of primary interest to chemists since reaction rates depend mainly on temperature for almost all systems, although there may also be some weaker pressure dependence. Measuring temperature accurately in the core can be problematic because of the presence of a thermal boundary layer; see the comments below on roll-up vortices. However, with the experimental pressure data in hand, the corresponding temperatures can be estimated using the isentropic relation

$$\ln(p/p_i) = \int_{T_i}^T \frac{\gamma(s)}{s(\gamma(s) - 1)} ds, \quad (1)$$

where (T_i, p_i) are the initial values for the core temperature and pressure, (T, p) are these quantities at some later time, and $\gamma(s)$ is the specific heat ratio at temperature s . In experiments, the initial core temperature is typically $O(300)$ K, while the core temperature after compression is usually $O(1000)$ K.

In this paper, we shall consider only the behaviour of the gas mixture during compression; the post-compression behaviour is not considered here, but this will form the subject for future work. Nevertheless, the model presented here does provide a reasonable description of the post-compression behaviour of a single species pure gas, or an inert gas mixture; see Section 3.5.

1.2. THE MODEL

We suppose that the compression chamber is located along $0 < x < 2L$ at $t = 0$, with $x = 0$ giving the initial location of the left piston and $x = 2L$ being the initial location of the right piston. It is assumed throughout this paper that the gas motion is one-dimensional so that the flow variables depend only on the position x along the chamber and time $t > 0$. This assumption is actually quite a strong one in this context since higher-dimensional effects are frequently observed in experiments, roll-up vortices near the corner regions defined by the piston heads and the chamber wall being particularly noteworthy; see, for example, [5]. These vortices arise due to the scraping by the pistons of the thermal boundary layer at the chamber wall, and they can, and frequently do, disturb the gas motion in the core of the compression chamber. However, the justification for the one-dimensional model studied here is twofold: (i) the corner vortices can be successfully suppressed by introducing crevices at the piston heads which swallow the thermal boundary layer as the pistons move in (see Lee [6]), rendering the gas motion away from the chamber walls one-dimensional to a good approximation, and, (ii) the study of the one-dimensional model provides a useful preliminary to the study of higher-dimensional models.

We now give the governing equations for our one-dimensional model. A reasonably complete derivation of the governing equations for a multi-component reacting gas can be found in the appendices of [7]; these standard derivations are not reproduced here. The model which we shall study includes a number of simplifying assumptions and these will be clearly stated as they arise.

The equation expressing conservation of mass is given by

$$\frac{\partial \rho}{\partial t} + \frac{\partial}{\partial x}(\rho v) = 0,$$

where $\rho = \rho(x, t)$ and $v = v(x, t)$ are the density and the velocity of the gas, respectively, at location x and time t . It should be emphasized that these quantities refer to a gas mixture, so that if there are N different species in the mixture then

$$\rho = \sum_{i=1}^N \rho_i,$$

where $\rho_i = \rho_i(x, t)$ is the density of species i . Also, the velocity v above refers to the mass-averaged velocity of the mixture, that is,

$$v = \sum_{i=1}^N Y_i v_i,$$

where $Y_i = \rho_i/\rho$ and $v_i = v_i(x, t)$ are the mass fraction and velocity, respectively, of species i ; see [7].

Neglecting body forces and viscous effects, the equation expressing conservation of momentum is given by

$$\frac{\partial v}{\partial t} + v \frac{\partial v}{\partial x} = -\frac{1}{\rho} \frac{\partial p}{\partial x},$$

where $p = p(x, t)$ is the pressure. We assume that the gas mixture is ideal, so that the equation of state is given by

$$p = \frac{R}{M} \rho T, \quad (2)$$

where $T = T(x, t)$ is the temperature, R is the universal gas constant ($8.314 \text{ JK}^{-1} \text{ mol}^{-1}$), and M is the average molecular mass of the mixture. This last quantity is given by

$$M = \sum_{i=1}^N n_i W_i (mA),$$

where n_i and W_i give the number fraction and molecular weight, respectively, of species i , m is the atomic mass unit ($1.661 \times 10^{-27} \text{ kg}$) and A is Avogadro's number ($6.022 \times 10^{23} \text{ molecules mol}^{-1}$).

The equation expressing conservation of energy is given by (see [7] or [8])

$$\rho \left(\frac{\partial u}{\partial t} + v \frac{\partial u}{\partial x} \right) = -M \left(\frac{\partial q}{\partial x} + p \frac{\partial v}{\partial x} \right), \quad (3)$$

where $u = u(x, t)$ is the internal energy of the gas mixture and $q = q(x, t)$ is the heat flux. We also have the thermodynamic identity

$$u = \sum_{i=1}^N h_i Y_i - Mp/\rho, \quad (4)$$

where the enthalpies $h_i = h_i(T)$ are given by

$$h_i(T) = h_i(T^0) + \int_{T^0}^T c_{p,i}(s) ds, \quad i = 1, 2, \dots, N, \quad (5)$$

where T^0 is some reference temperature and the $c_{p,i}(T)$ are the specific heats at constant pressure for the N species. When diffusion velocities and the radiant heat (again, see [7] for more details) are neglected, the expression for the heat flux is given by

$$q = -\lambda(T) \frac{\partial T}{\partial x}, \quad (6)$$

where $\lambda(T)$ is the thermal conductivity.

The mass fractions $Y_i = \rho_i/\rho$ are not necessarily constant since chemical reactions can change the composition of the mixture. However, for many systems such chemical effects can be neglected in the analysis of the compression because the gas mixture is ‘cold’ for most of the compression time. The core temperature will only rise to a level where chemical reactions can have a significant effect near the end of the compression, and the duration of this period is typically very short (a couple of milliseconds usually). Nevertheless, it is possible for some chemical reactions to proceed sufficiently rapidly for them to significantly influence the compression behaviour. However, we do not attempt to model systems which exhibit this behaviour here and take the Y_i to be constant during compression.

Substituting (4) and (6) in (3), and using (5), we have the final form of the equation expressing conservation of energy:

$$\frac{\partial T}{\partial t} + v \frac{\partial T}{\partial x} = \frac{M}{\rho(c_p(T) - R)} \left(\frac{\partial}{\partial x} \left(\lambda(T) \frac{\partial T}{\partial x} \right) - p \frac{\partial v}{\partial x} \right),$$

where

$$c_p = \sum_{i=1}^N Y_i c_{p,i}$$

is the mass-averaged specific heat.

1.3. BOUNDARY AND INITIAL CONDITIONS

We suppose that the left and right pistons move with constant velocities V_0 and $-V_0$, respectively, so that their motions are given by $x = V_0 t$ and $x = 2L - V_0 t$. In reality, the pistons in a rapid-compression machine will spend some of the compression time accelerating from rest and decelerating to rest, and this is not difficult to incorporate into the analysis given below. However, rather than complicate the analysis unnecessarily at the outset by considering variable piston velocity, we shall simply quote the results for general piston motion once the constant velocity case has been completed; see Section 3.4. Throughout the compression, we assume that the temperature of the walls of the chamber remain at their initial constant value, which we denote by T_0 . Hence, at the left piston, we impose

$$v = V_0, \quad T = T_0 \text{ on } x = V_0 t,$$

while at the right piston we set

$$v = -V_0, \quad T = T_0 \text{ on } x = 2L - V_0 t.$$

The gas in the chamber is initially at rest and we suppose that

$$v = 0, \quad T = T_0, \quad p = p_0, \quad \rho = \rho_0 \text{ at } t = 0,$$

where p_0 and ρ_0 are constants. Clearly, in view of (2), we have

$$p_0 = \frac{R}{M} \rho_0 T_0.$$

However, the above are not quite the boundary and initial conditions that are considered in this paper. For the conditions described above we have the symmetry

$$\begin{aligned} v(x, t) &= -v(2L - x, t), \quad T(x, t) = T(2L - x, t), \quad p(x, t) = p(2L - x, t), \\ \rho(x, t) &= \rho(2L - x, t). \end{aligned}$$

We exploit this behaviour by halving the spatial domain, considering the gas motion in $V_0 t < x < L$, and imposing symmetry conditions for the velocity and temperature on the centre-line, that is,

$$v = 0, \quad \frac{\partial T}{\partial x} = 0 \text{ on } x = L. \quad (7)$$

The appropriate conditions for a single-piston machine are very similar to those for a two-piston machine, the only difference arising at the right end where we now have

$$v = 0, \quad T = T_0 \text{ on } x = L,$$

instead of (7). The analysis of this problem is also very similar to that of the two-piston case, the principal difference now being that there is a thermal boundary layer at $x = L$ as well as at $x = V_0 t$. However, for the asymptotic analysis given below, the leading-order behaviour in the core region (the outer region) is identical for both sets of boundary conditions, and the algorithm presented in Section 3.4 is applicable to both problems.

1.4. NON-DIMENSIONALIZATION

We define the non-dimensional variables

$$\begin{aligned} \bar{x} &= \frac{x}{L}, \quad \bar{t} = \frac{t}{(L/V_0)}, \quad \bar{v} = \frac{v}{V_0}, \quad \bar{p} = \frac{p}{p_0}, \\ \bar{\rho} &= \frac{\rho}{\rho_0}, \quad \bar{T} = \frac{T}{T_0}, \quad \bar{\gamma}(\bar{T}) = \frac{c_p(T)}{c_p(T) - R}, \quad \bar{\lambda}(\bar{T}) = \frac{\lambda(T)}{\lambda(T_0)}, \end{aligned}$$

to obtain the following non-dimensional problem, upon dropping the overbars for convenience,

$$\begin{aligned} p &= \rho T, \\ \frac{\partial \rho}{\partial t} + \frac{\partial}{\partial x}(\rho v) &= 0, \\ \frac{\partial v}{\partial t} + v \frac{\partial v}{\partial x} &= -\frac{\theta}{\rho} \frac{\partial p}{\partial x}, \\ \rho \left(\frac{\partial T}{\partial t} + v \frac{\partial T}{\partial x} \right) &= (\gamma(T) - 1) \left(\varepsilon \frac{\partial}{\partial x} \left(\lambda(T) \frac{\partial T}{\partial x} \right) - p \frac{\partial v}{\partial x} \right), \\ v = 1, \quad T = 1 &\text{ on } x = t, \\ v = 0, \quad \frac{\partial T}{\partial x} &= 0 \text{ on } x = 1, \\ v = 0, \quad T = 1, \quad p = 1, \quad \rho = 1 &\text{ at } t = 0, \end{aligned} \quad (8)$$

Table 1. Values of $(\varepsilon, 1/\theta, \gamma(T_0))$ for some gases with $V_0 = 10 \text{ ms}^{-1}$, $T_0 = 300 \text{ K}$, $p_0 = 0.06 \text{ MPa}$ and $L = 0.25 \text{ m}$; the data was compiled from [9] and [10].

Gas	ε	$1/\theta$	$\gamma(T_0)$
Oxygen (O ₂)	5.3×10^{-5}	1.3×10^{-3}	1.39
Methane (CH ₄)	6.8×10^{-5}	6.4×10^{-4}	1.30
Carbon Dioxide (CO ₂)	3.3×10^{-5}	1.8×10^{-3}	1.29
Nitric Oxide (NO)	5.2×10^{-5}	1.2×10^{-3}	1.39

where the non-dimensional parameters θ and ε are given by

$$\theta = \frac{p_0}{\rho_0 V_0^2} = \frac{RT_0}{MV_0^2}, \quad \varepsilon = \frac{\lambda(T_0)T_0}{L V_0 p_0}.$$

For many gases and gas mixtures, $\gamma(T)$ is to a good approximation linear or constant, so we consider the particular form

$$\gamma(T) = \gamma_0 + \gamma_1 T, \quad (9)$$

where γ_0 and γ_1 are constants. In the numerical results discussed below, we use constant values for λ and γ . Under typical experimental conditions, $\varepsilon \ll 1/\theta \ll 1$, with $\varepsilon = O(10^{-5})$ and $1/\theta = O(10^{-3})$ frequently, see Table 1.

It is clear from Table 1 that the appropriate limit to consider in an asymptotic analysis of (8) is $\varepsilon \rightarrow 0$. However, there are a small number of exceptions to this - for very light gases such as Hydrogen and Helium, we have $1/\theta \ll \varepsilon \ll 1$ rather than $\varepsilon \ll 1/\theta \ll 1$. We shall see below that it is only necessary to consider the limit $\varepsilon \rightarrow 0$ in order to obtain usable results; the consideration of the subsequent limit $\theta \rightarrow \infty$ is not necessary, although we do very occasionally exploit the fact that θ is large.

2. Numerical solutions

2.1. THE NUMERICAL METHOD

The Equations (8) were numerically integrated by means of a finite-difference technique which explicitly time-stepped the solution from the initial data on a uniform mesh. Using forward difference approximations for the time derivatives, we used Equations (8)₂, (8)₃ and (8)₄ to explicitly time-step for ρ , v and T , respectively, Equation (8)₁ then being used to update the values for p . Backward finite differences were used to estimate the first spatial derivatives multiplying the velocity v , this choice corresponding to upwinding since $v \geq 0$. All of the numerical solutions were calculated using the values $\lambda(T) \equiv 1$, $\gamma(T) \equiv 1.9$, $\theta = 10$ and $\varepsilon = 8 \times 10^{-5}$. We should note that the value used for θ is significantly smaller than that for typical gases (see Table 1), and was chosen so as to emphasize the asymptotic behaviour as $\varepsilon \rightarrow 0$, while at the same time indicating the behaviour for large θ ; this is discussed in greater detail in Section 2.2. Centred differences were used to approximate $\partial^2 T / \partial x^2$.

In the numerical calculations, 250 uniformly spaced grid points along $0 \leq x \leq 1$ were used, with $\Delta t / \Delta x = 1/80$, where Δx is the space-step and Δt is the time-step. The piston

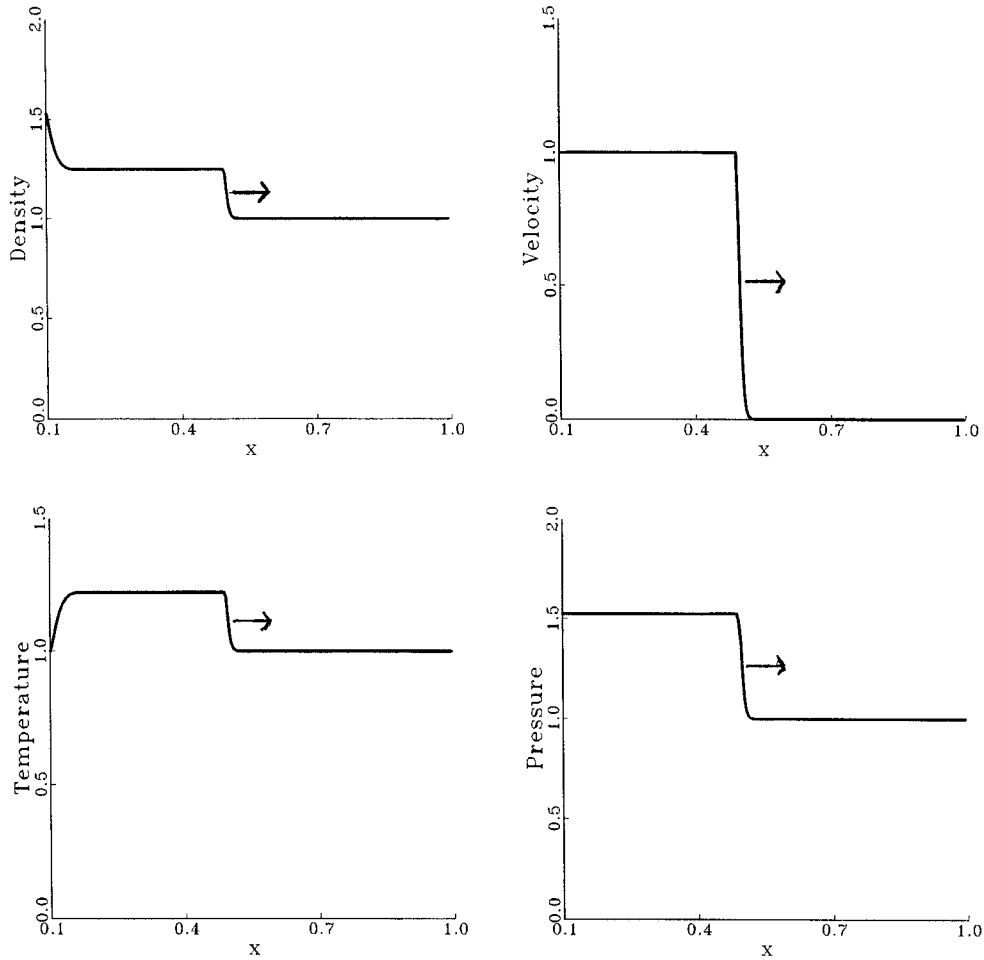


Figure 3. Numerical solution of (8) at $t = 0.1$ with $\gamma(T) \equiv 1.9$, $\lambda(T) \equiv 1$, $\theta = 10$ and $\varepsilon = 8 \times 10^{-5}$.

motion, $x = t$, was simulated by moving the left edge of the domain in one grid point every 80 time-steps, starting at the 40th time-step; this was found to represent adequately the motion of the piston. More general piston motions, $x = X_p(t)$, can be dealt with similarly without much difficulty.

2.2. DISCUSSION OF THE NUMERICAL RESULTS

Some numerical solutions of (8) are displayed in Figures 3–5. Many of the comments which are made here about these solutions are based on the results of the asymptotic analysis given in Section 3. The aim of presenting the material in this order is to make the purpose and detail of the coming asymptotic analysis clearer.

When the compression starts, a (sound) wave moves rapidly off the head of the piston. It is shown in the next section that the speed of this wave is $O(\sqrt{\theta})$ for $\theta \gg 1$, and in view of the fact that $\theta = O(10^3)$ typically, the wave is usually of the order of 30 times faster than the piston. The time it takes the wave to reach the centre-line, $x = 1$, from which it is reflected, is $O(1/\sqrt{\theta})$. In Figure 3 we display a numerical solution corresponding to the first traverse of the wave down the chamber towards the centre-line. Ahead of the wave-front the gas is

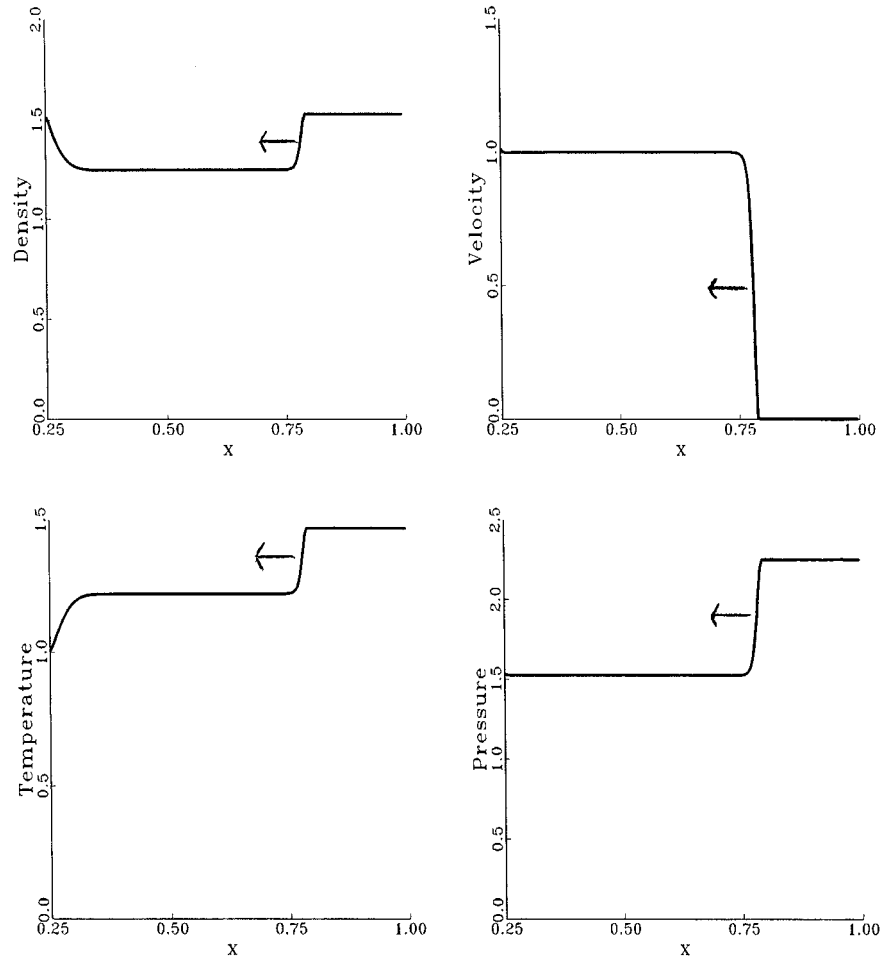


Figure 4. Numerical solution of (8) at $t = 0.25$ with $\gamma(T) \equiv 1.9$, $\lambda(T) \equiv 1$, $\theta = 10$ and $\varepsilon = 8 \times 10^{-5}$.

undisturbed and we have $v = 0$, $p = \rho = T = 1$ there. Behind the wave-front, it is found that $v \sim 1$ as $\varepsilon \rightarrow 0$, which means that, to leading order, the gas behind the wave is moving at the same velocity as the piston. In this region, it is also found that (p, ρ, T) are constant to leading order, and the asymptotic analysis readily yields the values for these constants. It is found that the wave carries with it an increase in (p, ρ, T) which is $O(1/\sqrt{\theta})$.

In Figure 3, the increase in (p, ρ, T) carried by the wave is quite significant because we have used $\theta = 10$, which is only moderately large; we chose not to use a very large value for θ so as not to obscure the asymptotic behaviour as $\varepsilon \rightarrow 0$. It should be emphasized that, for realistic values of θ ($\theta = O(10^3)$), the wave carries with it only a slight increase in (p, ρ, T) . However, because the wave speed is $O(\sqrt{\theta})$, the wave will typically pass through a particular point of the final chamber a large number of times for a given compression, giving rise to a very substantial increase in (p, ρ, T) by the end of the compression; these comments will be made precise by the forthcoming analysis.

There is an identical wave moving in the opposite direction from the piston on the right-hand side. When the two approaching waves collide at the centre-line, they reflect off each other, and in Figure 4 we display a numerical solution corresponding to a time when the

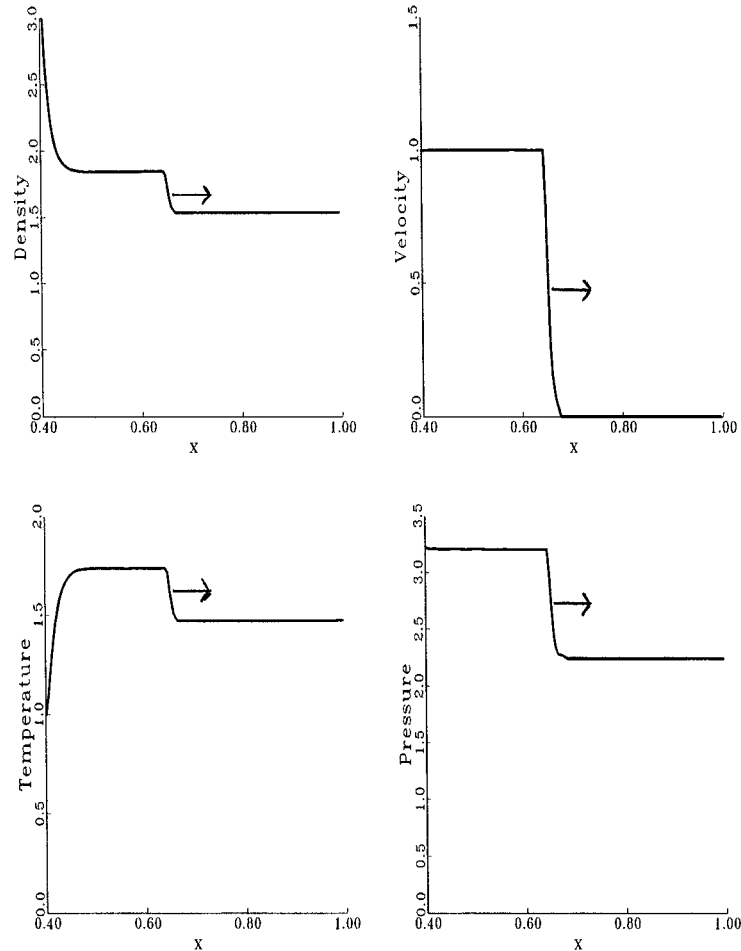


Figure 5. Numerical solution of (8) at $t = 0.40$ with $\gamma(T) \equiv 1.9$, $\lambda(T) \equiv 1$, $\theta = 10$ and $\varepsilon = 8 \times 10^{-5}$.

wave has reflected off the centre-line for the first time. The wave is now moving from right to left and again carries with it an increase in (p, ρ, T) which is $O(1/\sqrt{\theta})$. The leading-order constant values for (p, ρ, T) ahead of the wave-front are known, and the asymptotics enable us to calculate the constant leading order values for (p, ρ, T) behind the wave-front. When the wave reaches the piston, it reflects off it, and we again have a wave travelling from left to right towards the centre-line, the leading-order constant values for (p, ρ, T) behind the wave-front again being calculable. The process continues in this manner with the wave moving over and back in the chamber a large number of times during the compression, the new constant leading-order values for (p, ρ, T) which it carries with it during each pass of the wave being calculable.

2.3. DESCRIPTION OF THE ALGORITHM

We denote the initial values for (p, ρ, T) in the chamber core by (p_0, ρ_0, T_0) , and for our non-dimensionalization we have $p_0 = \rho_0 = T_0 = 1$. We associate the time $t_0 = 0$ with these values. When the wave leaves the piston head for the first time, we denote the leading-order constant values for (p, ρ, T) behind the wave-front by (p_1, ρ_1, T_1) (these can be calculated),

and the time we associate with these values, denoted by t_1 , is the time it takes the wave-front to reach the centre-line of the chamber; this time can be calculated since the asymptotics yield expressions for the speed of the wave. We denote the constant leading-order values for (p, ρ, T) behind the wave which is reflected from the centre-line by (p_2, ρ_2, T_2) and the time we associate with these values, denoted by t_2 , is t_1 plus the time it takes the reflected wave to return to the piston. Continuing in this way we can calculate a sequence of values (p_i, ρ_i, T_i, t_i) for $i = 1, 2, \dots$, which model the evolution of the pressure, density and temperature in the core of the chamber.

3. Asymptotic analysis; the algorithm

We now consider the asymptotic behaviour of (8) in the limit $\varepsilon \rightarrow 0$. We begin by considering the particular case when the wave travels down the chamber and reflects from the centre-line for the first time. The analysis of the case when the wave is travelling up and down the chamber for the N^{th} time is very similar, and we shall simply quote the relevant results once the $N = 1$ case has been completed.

The conditions associated with a rapid-compression event are very particular because of the short time-scales involved, and the very high final temperatures and pressures achieved. We are unaware of any previous studies of the kind given below for the behaviour of a gas mixture in a rapid compression machine. However, the calculation of jump conditions across normal shock-waves is very well established and is discussed in, for example, [11–13]. The use of singular perturbation theory to calculate jump conditions by matching across narrow transition layers is discussed in [14] and [15], among other textbooks on perturbation methods.

The asymptotic solutions presented below are formal, and have not been rigorously justified. A rigorous mathematical treatment of these issues would be of considerable value, but this is not the aim of the analysis presented in this paper.

3.1. THE FIRST PASS OF THE WAVE DOWN THE CHAMBER

3.1.1. Thermal boundary layer at the piston

This boundary layer is located near the piston and is clearly visible in the density and temperature profiles of the numerical solutions displayed in Figures 3–5; it arises because the piston head is assumed to remain fixed at its initial temperature throughout the compression, while in the chamber core the temperature increases significantly. The temperature rises from the fixed wall value to the temperature in the core over the boundary layer.

The layer is located at $\hat{x} = O(1)$, $\hat{x} \geq 0$, where $x = t + \varepsilon^{1/2}\hat{x}$, and in the variables (\hat{x}, t) the governing equations (8)₂, (8)₃ and (8)₄ become

$$\begin{aligned} \varepsilon^{1/2} \frac{\partial \rho}{\partial t} - \frac{\partial \rho}{\partial \hat{x}} + \frac{\partial}{\partial \hat{x}}(\rho v) &= 0, \\ \varepsilon^{1/2} \frac{\partial v}{\partial t} + (v - 1) \frac{\partial v}{\partial \hat{x}} &= -\frac{\theta}{\rho} \frac{\partial p}{\partial \hat{x}}, \\ \rho \left(\varepsilon^{1/2} \frac{\partial T}{\partial t} + (v - 1) \frac{\partial T}{\partial \hat{x}} \right) &= (\gamma(T) - 1) \left(\varepsilon^{1/2} \frac{\partial}{\partial \hat{x}} \left(\lambda(T) \frac{\partial T}{\partial \hat{x}} \right) - p \frac{\partial v}{\partial \hat{x}} \right). \end{aligned}$$

It is found that, in order to fully pose the leading-order problem in $\hat{x} = O(1)$, it is necessary to consider the first correction terms in the asymptotic expansions. However, we shall only

pursue these terms to the extent that they are required to pose the leading-order problem. Hence, in $\hat{x} = O(1)$, we pose (these scalings provide the consistent balance)

$$\begin{aligned} p &\sim \hat{p}_0(\hat{x}, t) + \varepsilon \hat{p}_1(\hat{x}, t), \quad \rho \sim \hat{\rho}_0(\hat{x}, t) + \varepsilon^{1/2} \hat{\rho}_1(\hat{x}, t), \\ v &\sim \hat{v}_0(\hat{x}, t) + \varepsilon^{1/2} \hat{v}_1(\hat{x}, t), \quad T \sim \hat{T}_0(\hat{x}, t) + \varepsilon^{1/2} \hat{T}_1(\hat{x}, t), \end{aligned}$$

as $\varepsilon \rightarrow 0$.

3.1.1.1. $O(1)$ equations:

These are

$$\begin{aligned} \hat{p}_0 &= \hat{\rho}_0 \hat{T}_0, \\ -\frac{\partial \hat{\rho}_0}{\partial \hat{x}} + \frac{\partial}{\partial \hat{x}} (\hat{\rho}_0 \hat{v}_0) &= 0, \\ (\hat{v}_0 - 1) \frac{\partial \hat{v}_0}{\partial \hat{x}} &= -\frac{\theta}{\hat{\rho}_0} \frac{\partial \hat{p}_0}{\partial \hat{x}}, \\ \hat{\rho}_0 (\hat{v}_0 - 1) \frac{\partial \hat{T}_0}{\partial \hat{x}} &= -(\gamma(\hat{T}_0) - 1) \hat{p}_0 \frac{\partial \hat{v}_0}{\partial \hat{x}}. \end{aligned} \tag{10}$$

Integrating (10)₂ and imposing the boundary condition $\hat{v}_0 = 1$ on $\hat{x} = 0$, we have

$$\hat{v}_0 = 1,$$

and (10)₃ then implies that

$$\frac{\partial \hat{p}_0}{\partial \hat{x}} = 0 \Rightarrow \hat{p}_0 = P_s(t),$$

where $P_s(t)$ will be determined below by matching. Notice now that Equation (10)₄ is identically satisfied and does not provide an equation for determining \hat{T}_0 . Hence the necessity of considering correction terms.

3.1.1.2. $O(\varepsilon^{1/2})$ equations:

These are

$$\begin{aligned} \hat{\rho}_0 \hat{T}_1 + \hat{\rho}_1 \hat{T}_0 &= 0, \\ \frac{\partial \hat{\rho}_0}{\partial t} + \frac{\partial}{\partial \hat{x}} (\hat{\rho}_0 \hat{v}_1) &= 0, \\ \hat{\rho}_0 \left(\frac{\partial \hat{v}_1}{\partial t} + \hat{v}_1 \frac{\partial \hat{v}_1}{\partial \hat{x}} \right) &= -\theta \frac{\partial \hat{p}_1}{\partial \hat{x}}, \\ \hat{\rho}_0 \left(\frac{\partial \hat{T}_0}{\partial t} + \hat{v}_1 \frac{\partial \hat{T}_0}{\partial \hat{x}} \right) &= (\gamma(\hat{T}_0) - 1) \left(\frac{\partial}{\partial \hat{x}} \left(\lambda(\hat{T}_0) \frac{\partial \hat{T}_0}{\partial \hat{x}} \right) - \hat{p}_0 \frac{\partial \hat{v}_1}{\partial \hat{x}} \right). \end{aligned} \tag{11}$$

Equation (11)₂ can be integrated for \hat{v}_1 to give

$$\hat{v}_1 = -\frac{1}{\hat{\rho}_0} \int_0^{\hat{x}} \frac{\partial \hat{\rho}_0(s, t)}{\partial t} ds, \quad (12)$$

where we have used the boundary condition $\hat{v}_1 = 0$ on $\hat{x} = 0$. Substituting (12) in (14)₄, and using $\hat{\rho}_0 = P_s(t)/\hat{T}_0$, we obtain

$$\begin{aligned} & \frac{P_s(t)}{\hat{T}_0} \frac{\partial \hat{T}_0}{\partial t} - \left\{ \int_0^{\hat{x}} \frac{\partial}{\partial t} \left(\frac{P_s(t)}{\hat{T}_0(s, t)} \right) ds \right\} \frac{\partial \hat{T}_0}{\partial \hat{x}} = \\ & (\gamma(\hat{T}_0) - 1) \left(\frac{\partial}{\partial \hat{x}} \left(\lambda(\hat{T}_0) \frac{\partial \hat{T}_0}{\partial \hat{x}} \right) + \frac{\partial}{\partial \hat{x}} \left(\hat{T}_0 \int_0^{\hat{x}} \frac{\partial}{\partial t} \left(\frac{P_s(t)}{\hat{T}_0(s, t)} \right) ds \right) \right), \end{aligned} \quad (13)$$

which is to be solved subject to

$$\begin{aligned} & \hat{T}_0 = 1 \text{ on } \hat{x} = 0, \\ & \hat{T}_0 = 1 \text{ at } t = 0, \\ & \hat{T}_0 \rightarrow T_c(t) \text{ as } \hat{x} \rightarrow +\infty, \end{aligned} \quad (14)$$

where $T_c(t)$ will be determined below by matching. This completes the specification of the leading-order problem in $\hat{x} = O(1)$, apart from $P_s(t)$ and $T_c(t)$, both of which are determined below. The solution of (13) subject to (14) is not pursued here since it is not required for the solution of the leading-order outer problem, and it is the outer problem which provides the discrete algorithm for tracking the behaviour in the chamber core.

3.1.2. Outer region

We denote the location of the wave-front by $x = q^+(t; \varepsilon)$, so that for $x > q^+$, we have $v = 0$, $p = \rho = T = 1$. For $x < q^+$ we pose

$$p \sim p_0^-(x, t), \quad \rho \sim \rho_0^-(x, t), \quad v \sim v_0^-(x, t), \quad T \sim T_0^-(x, t),$$

to obtain the leading-order equations

$$\begin{aligned} & p_0^- = \rho_0^- T_0^-, \\ & \frac{\partial \rho_0^-}{\partial t} + \frac{\partial}{\partial x} (\rho_0^- v_0^-) = 0, \\ & \frac{\partial v_0^-}{\partial t} + v_0^- \frac{\partial v_0^-}{\partial x} = -\frac{\theta}{\rho_0^-} \frac{\partial p_0^-}{\partial x}, \\ & \rho_0^- \left(\frac{\partial T_0^-}{\partial t} + v_0^- \frac{\partial T_0^-}{\partial x} \right) = -(\gamma(T_0^-) - 1) p_0^- \frac{\partial v_0^-}{\partial x}. \end{aligned} \quad (15)$$

These equations are solved subject to matching conditions as $x \rightarrow t$ (see Section 3.1.1 above), and as $x \rightarrow q^+$ (see Section 3.1.3 below). The solution to (15) is simply

$$v_0^- = 1, \quad p_0^- = P_s(t),$$

with ρ_0^- , T_0^- satisfying

$$\frac{\partial \rho_0^-}{\partial t} + \frac{\partial \rho_0^-}{\partial x} = 0, \quad \frac{\partial T_0^-}{\partial t} + \frac{\partial T_0^-}{\partial x} = 0,$$

so that

$$\rho_0^- = f(x-t), \quad T_0^- = P_s(t)/f(x-t),$$

where $f(x-t)$ is determined below by matching as $x \rightarrow q^+$. This choice for the outer solution satisfies the governing equations (15) and will be seen to be consistent with the matching conditions at both ends; its consistency with the numerical solution presented in Figure 3 is already clear. We note that $T_c(t) = P_s(t)/f(0)$.

3.1.3. Transition region

This region is located at $z^* = O(1)$ where $x = q^+(t; \varepsilon) + \varepsilon z^*$. It is clearly visible in the numerical solution displayed in Figures 3, particularly in the profile for the velocity where it corresponds to the narrow region over which v drops from $v \sim 1$ to $v = o(1)$. In $z^* = O(1)$, we pose

$$q^+ \sim q_0^+(t), \quad p \sim p_0^*(z^*, t), \quad \rho \sim \rho_0^*(z^*, t), \quad v \sim v_0^*(z^*, t), \quad T \sim T_0^*(z^*, t),$$

to obtain the leading-order equations

$$\begin{aligned} p_0^* &= \rho_0^* T_0^*, \\ -\dot{q}_0^+ \frac{\partial \rho_0^*}{\partial z^*} + \frac{\partial}{\partial z^*} (\rho_0^* v_0^*) &= 0, \\ (v_0^* - \dot{q}_0^+) \frac{\partial v_0^*}{\partial z^*} &= -\frac{\theta}{\rho_0^*} \frac{\partial p_0^*}{\partial z^*}, \\ \rho_0^* (v_0^* - \dot{q}_0^+) \frac{\partial T_0^*}{\partial z^*} &= (\gamma(T_0^*) - 1) \left(\frac{\partial}{\partial z^*} \left(\lambda(T_0^*) \frac{\partial T_0^*}{\partial z^*} \right) - p_0^* \frac{\partial v_0^*}{\partial z^*} \right). \end{aligned} \tag{16}$$

We now integrate each of the Equations (16)₂, (16)₃ and (16)₄ in turn, first matching into the known data as $z^* \rightarrow +\infty$, and then considering the behaviour as $z^* \rightarrow -\infty$, to obtain relations between the outer solutions on the two sides of the wave-front. We recall that Equations (16)₂, (16)₃ and (16)₄ express conservation of mass, momentum and energy, respectively.

Integrating (16)₂, and imposing $v_0^* \rightarrow 0$, $\rho_0^* \rightarrow 1$ as $z^* \rightarrow +\infty$, we have

$$\rho_0^* = \frac{\dot{q}_0^+}{\dot{q}_0^+ - v_0^*}, \tag{17}$$

and letting $z^* \rightarrow -\infty$ in this expression gives

$$f(q_0^+ - t) = \frac{\dot{q}_0^+}{\dot{q}_0^+ - 1}.$$

We shall show below that \dot{q}_0^+ is in fact constant, so that, $f(x-t) \equiv \dot{q}_0^+ / (\dot{q}_0^+ - 1)$, and,

$$\rho_0^- = \frac{\dot{q}_0^+}{\dot{q}_0^+ - 1}, \tag{18}$$

a constant. Clearly, we require that $\dot{q}_0^+ - 1 > 0$, but this amounts to nothing more than requiring that the pistons travel at velocities which do not exceed the speed of sound in the gas. Recall that the maximum speed of the pistons is $O(10 \text{ ms}^{-1})$, while the speed of sound in gases under typical conditions is frequently $O(300 \text{ ms}^{-1})$.

Substituting (17) in (16)₃, and integrating subject to the conditions $v_0^* \rightarrow 0$, $p_0^* \rightarrow 1$ as $z^* \rightarrow +\infty$, we have

$$p_0^* = 1 + \dot{q}_0^+ v_0^*/\theta. \quad (19)$$

Letting $z^* \rightarrow -\infty$ in (19) we obtain

$$P_s(t) = 1 + \dot{q}_0^+/\theta, \quad (20)$$

so that,

$$T_c(t) = (1 + \dot{q}_0^+/\theta)(1 - 1/\dot{q}_0^+), \quad (21)$$

both of which are constant since, as we shall now show, \dot{q}_0^+ is constant. The prediction that (p, ρ, T) are constant to leading order in the outer region behind the wave-front is clearly consistent with the numerical solution displayed in Figure 3.

Substituting (17) and (19) in (16)₄ and integrating subject to $v_0^* \rightarrow 0$, $T_0^* \rightarrow 1$, $\partial T_0^*/\partial z^* \rightarrow 0$ as $z^* \rightarrow +\infty$, we get

$$-\dot{q}_0^+ \mu(T_0^*) = \lambda(T_0^*) \frac{\partial T_0^*}{\partial z^*} - (v_0^* + \dot{q}_0^+ v_0^{*2}/2\theta), \quad (22)$$

where

$$\mu(T_0^*) = \int_1^{T_0^*} \frac{ds}{\gamma(s) - 1}.$$

Letting $z^* \rightarrow -\infty$ in (22), we obtain

$$\dot{q}_0^+ \mu((1 + \dot{q}_0^+/\theta)(1 - 1/\dot{q}_0^+)) = 1 + \dot{q}_0^+/2\theta, \quad (23)$$

which determines \dot{q}_0^+ , completing the specification of the leading order outer problem. It is clear that the solution for \dot{q}_0^+ to (23) does not depend on t , so that q_0^+ has the form αt where α is a constant.

Using (9), we have

$$\mu(T_0^*) = \frac{1}{\gamma_1} \ln \left(\frac{\gamma_0 + \gamma_1 T_0^* - 1}{\gamma_0 + \gamma_1 - 1} \right),$$

so that (23) becomes

$$\frac{\dot{q}_0^+}{\gamma_1} \ln \left(\frac{\gamma_0 - 1 + \gamma_1(1 + \dot{q}_0^+/\theta)(1 - 1/\dot{q}_0^+)}{\gamma_0 + \gamma_1 - 1} \right) = 1 + \dot{q}_0^+/2\theta, \quad (24)$$

which is an equation that is easily solved numerically for \dot{q}_0^+ for given values of γ_0 , γ_1 and θ . In the limit $\gamma_1 \rightarrow 0$ (so that $\gamma(T) \equiv \gamma_0$) this expression reduces to a quadratic in \dot{q}_0^+ which can be solved to give

$$\dot{q}_0^+ = \frac{1}{4} \left(\gamma_0 + 1 \pm \sqrt{(\gamma_0 + 1)^2 + 16\gamma_0\theta} \right),$$

with the positive solution being clearly the relevant one here. The numerical solution of (24) for $\gamma_1 \neq 0$ is usually unnecessary. Recalling that $\theta = O(10^3)$ typically, and considering the behaviour of (24) for $\theta \gg 1$, we can easily show that

$$\dot{q}_0^+ \sim \sqrt{(\gamma_0 + \gamma_1)\theta} \text{ for } \theta \gg 1. \quad (25)$$

In dimensional terms, this expression for \dot{q}_0^+ is

$$\sqrt{\frac{\gamma(T_0)p_0}{\rho_0}},$$

which is the familiar expression for the speed of sound in an ideal gas. We favour the simpler expression (25) over (24) for the algorithm described in Section 3.4.

It is worth noting here that the relations (18), (20) and (23) could also have been obtained using integral forms for the conservation laws, and it is not necessary (although it is preferable) to consider the detail of the transition layer. For example, conservation of mass implies that

$$\frac{d}{dt} \left(\int_t^1 \rho(x, t) dx \right) = 0,$$

which at leading order gives

$$\frac{d}{dt} \left(\int_t^{q_0^+} \rho_0^-(x, t) dx + \int_{q_0^+}^1 1 dx \right) = 0,$$

and this leads to (18).

3.1.4. Summary

The motion of the wave-front, $x = q^+(t; \varepsilon)$, is such that as $\varepsilon \rightarrow 0$, $q^+(t; \varepsilon) \sim q_0^+(t)$, where $q_0^+(t)$ is determined by solving (24) subject to $q_0^+(0) = 0$. For $x < q^+$, we have as $\varepsilon \rightarrow 0$,

$$p \sim 1 + \dot{q}_0^+/\theta, \quad \rho \sim \dot{q}_0^+ / (\dot{q}_0^+ - 1), \quad v \sim 1, \quad T \sim (1 + \dot{q}_0^+/\theta)(1 - 1/\dot{q}_0^+), \quad (26)$$

all of which are known constants. For $x > q^+$, $p = \rho = T = 1$ and $v = 0$.

3.2. THE FIRST REFLECTION OF THE WAVE FROM THE CENTRE-LINE

When the wave-front reaches the centre-line, it reflects off the identical opposing wave, and then moves from right to left towards the incoming piston. The leading-order behaviour ahead of the wave is now known from the calculations of the previous subsection. A numerical solution illustrating this case is given in Figure 4. The leading-order behaviour in the boundary layer near the piston is clearly unchanged from that considered in Section 3.1.1 and requires no further discussion.

3.2.1. Outer region

We denote the motion of the reflected wave by $x = q^-(t; \varepsilon)$. For $x < q^-$, equations (26) hold. For $x > q^-$, we have $v = o(1)$ and we pose

$$p \sim p_0^+(x, t), \quad \rho \sim \rho_0^+(x, t), \quad T \sim T_0^+(x, t)$$

to obtain

$$p_0^+ = \rho_0^+ T_0^+, \quad \frac{\partial \rho_0^+}{\partial t} = 0, \quad \frac{\partial p_0^+}{\partial x} = 0, \quad \frac{\partial T_0^+}{\partial t} = 0,$$

so that

$$p_0^+ = P_{sr}, \quad \rho_0^+ = g(x), \quad T_0^+ = P_{sr}/g(x),$$

where P_{sr} , which is constant, and $g(x)$ are determined below by matching.

3.2.2. Transition region

This is located at $z^\dagger = O(1)$ where $x = q^-(t; \varepsilon) + \varepsilon z^\dagger$. It gives the location of the narrow region over which v drops from $v \sim 1$ to $v = o(1)$; the transition region is also clearly identifiable in the solutions for p , ρ and T ; see Figure 4. In $z^\dagger = O(1)$ we pose

$$q^- \sim q_0^-(t), \quad p \sim p_0^\dagger(z^\dagger, t), \quad \rho \sim \rho_0^\dagger(z^\dagger, t), \quad v \sim v_0^\dagger(z^\dagger, t), \quad T \sim T_0^\dagger(z^\dagger, t),$$

to obtain leading-order equations which have precisely the same form as (16). Integrating and matching in a manner similar to that described in Section 3.1.3, we obtain

$$\begin{aligned} \rho_0^\dagger &= \frac{\dot{q}_0^+(\dot{q}_0^- - 1)}{(\dot{q}_0^+ - 1)(\dot{q}_0^- - v_0^\dagger)}, \\ v_0^\dagger &= 1 + \frac{\theta(\dot{q}_0^+ - 1)}{\dot{q}_0^+(\dot{q}_0^- - 1)}(p_0^\dagger - 1 - \dot{q}_0^+/\theta), \\ \frac{\dot{q}_0^+(\dot{q}_0^- - 1)}{\dot{q}_0^+ - 1}(\mu(T_c) - \mu(T_0^\dagger)) &= \\ \lambda(T_0^\dagger) \frac{\partial T_0^\dagger}{\partial z^\dagger} - \left((1 + \dot{q}_0^+/\theta)(v_0^\dagger - 1) + \frac{\dot{q}_0^+(\dot{q}_0^- - 1)}{2\theta(\dot{q}_0^+ - 1)}(v_0^{\dagger 2} - 1) \right). \end{aligned} \quad (27)$$

Letting $z^\dagger \rightarrow +\infty$ in (27) gives

$$\begin{aligned} g(x) &\equiv \frac{\dot{q}_0^+(\dot{q}_0^- - 1)}{\dot{q}_0^-(\dot{q}_0^+ - 1)}, \quad P_{sr} = 1 + \frac{\dot{q}_0^+(\dot{q}_0^+ - \dot{q}_0^-)}{\theta(\dot{q}_0^+ - 1)}, \\ T_0^+ &= \frac{\dot{q}_0^-}{\dot{q}_0^+(\dot{q}_0^- - 1)} \left(\dot{q}_0^+ - 1 + \frac{\dot{q}_0^+}{\theta}(\dot{q}_0^+ - \dot{q}_0^-) \right), \end{aligned} \quad (28)$$

where the constant reflected wave speed \dot{q}_0^- is determined as the negative solution to

$$\frac{\dot{q}_0^+(\dot{q}_0^- - 1)}{\gamma_1(\dot{q}_0^+ - 1)} \ln \left(\frac{\gamma_0 - 1 + \gamma_1 T_c}{\gamma_0 - 1 + \gamma_1 T_0^+} \right) = 1 + \frac{\dot{q}_0^+}{\theta} - \frac{\dot{q}_0^+(\dot{q}_0^- - 1)}{2\theta(\dot{q}_0^+ - 1)}, \quad (29)$$

where T_c is given by (21) and T_0^+ is given in (28). Considering the behaviour of this last expression for $\theta \gg 1$, we find that $\dot{q}_0^- \sim \pm \sqrt{(\gamma_0 + \gamma_1)\theta}$, the negative solution being the relevant one now. It is this simpler form which we shall use for the algorithm described in Section 3.4.

3.2.3. Summary

The location of the reflected wave-front, $x = q^-(t; \varepsilon)$, is such that as $\varepsilon \rightarrow 0$, $q^-(t; \varepsilon) \sim q_0^-(t)$, where $\dot{q}_0^-(t)$ is determined as the solution to (29). For $x < q^-$, the leading-order solutions are given by (26). For $x > q^-$, we have $v = o(1)$ and

$$\begin{aligned} p &\sim 1 + \frac{\dot{q}_0^+(\dot{q}_0^+ - \dot{q}_0^-)}{\theta(\dot{q}_0^+ - 1)}, \quad \rho \sim \frac{\dot{q}_0^+(\dot{q}_0^- - 1)}{\dot{q}_0^-(\dot{q}_0^+ - 1)}, \\ T &\sim \frac{\dot{q}_0^-}{\dot{q}_0^+(\dot{q}_0^- - 1)} \left(\dot{q}_0^+ - 1 + \frac{\dot{q}_0^+}{\theta}(\dot{q}_0^+ - \dot{q}_0^-) \right). \end{aligned}$$

3.3. THE WAVE TRAVELS OVER AND BACK IN THE CHAMBER FOR THE N^{th} TIME

Most of the notation required here has previously been introduced in Section 2.3.

3.3.1. *The wave travels down the chamber for the N^{th} time*

Denoting the location of the wave-front by q_N^+ , we have for $x < q_N^+$,

$$q_N^+ \sim q_{N0}^+, \quad p \sim p_{2N-1}, \quad \rho \sim \rho_{2N-1}, \quad v \sim 1, \quad T \sim T_{2N-1},$$

as $\varepsilon \rightarrow 0$, with $(p_{2N-1}, \rho_{2N-1}, T_{2N-1})$ constant. For $x > q_N^+$, we have $v = o(1)$ and

$$p \sim p_{2N-2}, \quad \rho \sim \rho_{2N-2}, \quad T \sim T_{2N-2},$$

where $(p_{2N-2}, \rho_{2N-2}, T_{2N-2})$ are constants. If we now consider the transition layer of thickness $O(\varepsilon)$ about q_N^+ , and perform calculations which are almost identical to those of Section 3.1.3, we find that

$$\begin{aligned} \rho_{2N-1} &= \frac{\dot{q}_{N0}^+}{\dot{q}_{N0}^+ - 1} \rho_{2N-2}, \\ p_{2N-1} &= p_{2N-2} + \frac{\dot{q}_{N0}^+}{\theta} \rho_{2N-2}, \\ T_{2N-1} &= \frac{p_{2N-1}}{\rho_{2N-1}}, \\ \dot{q}_{N0}^+ \rho_{2N-2} (\mu(T_{2N-1}) - \mu(T_{2N-2})) &= p_{2N-2} + \frac{\dot{q}_{N0}^+}{2\theta} \rho_{2N-2}. \end{aligned} \tag{30}$$

Using (9), and considering the behaviour of (30)₄ for $\theta \gg 1$, we can easily show that

$$\dot{q}_{N0}^+ \sim \sqrt{\gamma(T_{2N-2}) T_{2N-2} \theta} = \sqrt{\frac{\gamma(T_{2N-2}) p_{2N-2} \theta}{\rho_{2N-2}}} \text{ for } \theta \gg 1.$$

We note from this expression that as the pistons compress the gas in the chamber core, the speed of the wave increases in proportion to the square root of the rising temperature (for $\gamma(T)$ constant). If $\gamma(T) \equiv \gamma_0$, then we can solve exactly for \dot{q}_{N0}^+ to obtain

$$\dot{q}_{N0}^+ = \frac{1}{4} \left(\gamma_0 + 1 + \sqrt{(\gamma_0 + 1)^2 + 16\gamma_0 \theta T_{2N-2}} \right). \tag{31}$$

3.3.2. *The wave reflects off the centre-line for the N^{th} time*

We denote the location of the wave-front by $x = q_N^-$. As $\varepsilon \rightarrow 0$, we have for $x < q_N^-$,

$$q_N^- \sim q_{N0}^-, \quad p \sim p_{2N-1}, \quad \rho \sim \rho_{2N-1}, \quad v \sim 1, \quad T \sim T_{2N-1}.$$

For $x > q_N^-$, we have $v = o(1)$ and

$$p \sim p_{2N}, \quad \rho \sim \rho_{2N}, \quad T \sim T_{2N},$$

with $(p_{2N}, \rho_{2N}, T_{2N})$ constant. Considering the transition layer about q_N^- , it is readily shown that

$$\begin{aligned}
 \rho_{2N} &= \frac{\dot{q}_{N0}^- - 1}{\dot{q}_{N0}^-} \rho_{2N-1}, \\
 p_{2N} &= p_{2N-1} - \frac{\dot{q}_{N0}^-}{\theta} \rho_{2N}, \\
 T_{2N} &= \frac{p_{2N}}{\rho_{2N}}, \\
 \dot{q}_{N0}^- \rho_{2N} (\mu(T_{2N-1}) - \mu(T_{2N})) &= p_{2N} + \frac{\dot{q}_{N0}^-}{2\theta} \rho_{2N}.
 \end{aligned} \tag{32}$$

Considering the behaviour of (34)₄ for $\theta \gg 1$, we have

$$\dot{q}_{N0}^- \sim -\sqrt{\gamma(T_{2N-1})T_{2N-1}\theta} = -\sqrt{\frac{\gamma(T_{2N-1})p_{2N-1}\theta}{\rho_{2N-1}}} \text{ for } \theta \gg 1.$$

For $\gamma(T) \equiv \gamma_0$, we have the exact expression

$$\dot{q}_{N0}^- = \frac{1}{4} \left(3 - \gamma_0 - \sqrt{(3 - \gamma_0)^2 + 16\gamma_0\theta T_{2N-1} + 8(\gamma_0 - 1)} \right). \tag{33}$$

3.4. THE ALGORITHM

3.4.1. Constant piston velocity

The calculations of the previous subsections yield the following simple iterative algorithm for the evolution of the pressure, density and temperature in the chamber core:

$$p_0 = \rho_0 = T_0 = 1, \quad t_0 = 0,$$

and for $N = 1, 2, 3, \dots$, we have

$$\begin{aligned}
 \dot{q}_N^+ &= \sqrt{\gamma(T_{2N-2})T_{2N-2}\theta}, & \rho_{2N-1} &= \frac{\dot{q}_N^+}{\dot{q}_N^+ - 1} \rho_{2N-2}, \\
 p_{2N-1} &= p_{2N-2} + \frac{\dot{q}_N^+}{\theta} \rho_{2N-2}, & T_{2N-1} &= \frac{p_{2N-1}}{\rho_{2N-1}}, \\
 t_{2N-1} &= t_{2N-2} + \frac{1 - t_{2N-2}}{\dot{q}_N^+}, & \dot{q}_N^- &= -\sqrt{\gamma(T_{2N-1})T_{2N-1}\theta}, \\
 \rho_{2N} &= \frac{\dot{q}_N^- - 1}{\dot{q}_N^-} \rho_{2N-1}, & p_{2N} &= p_{2N-1} - \frac{\dot{q}_N^-}{\theta} \rho_{2N}, \\
 T_{2N} &= \frac{p_{2N}}{\rho_{2N}}, & t_{2N} &= t_{2N-1} + \frac{1 - t_{2N-1}}{1 - \dot{q}_N^-}.
 \end{aligned} \tag{34}$$

It is clear that this iterative scheme is trivial to implement on a computer. Once a calculation based on this algorithm has been completed, one could, for example, plot the pressure in the chamber during compression by simply passing a smooth curve through the data points (p_i, t_i) , $i = 0, 1, 2, \dots$

In Figure 6(a), we have plotted curves through data points for (p_i, t_i) , (ρ_i, t_i) and (T_i, t_i) , as calculated using the algorithm (34). In experiments, the only quantity which is measured throughout the compression is the pressure. It is immediately obvious that the algorithm is

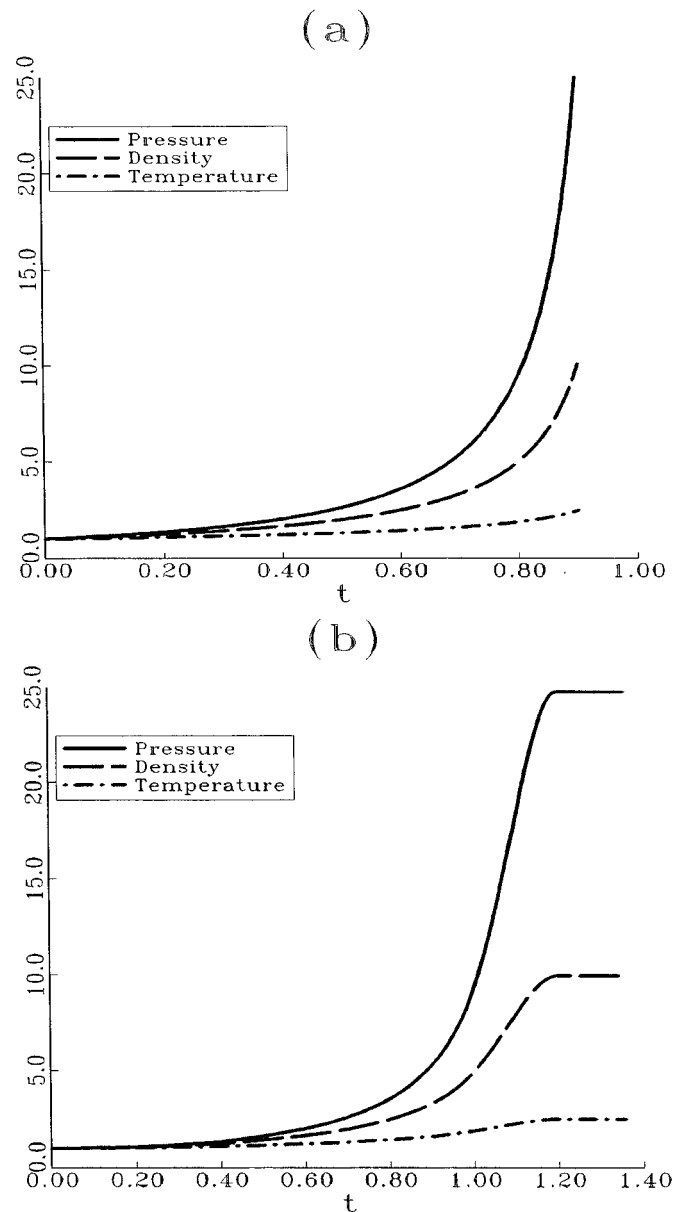


Figure 6. Pressure, temperature and density profiles in the chamber core as functions of time calculated using (a) the iterative scheme (34) which has $X_p(t) = t$, and (b) the iterative scheme (37) with $X_p(t)$ given by (38). In both cases, the values used were $\gamma(T) \equiv 1.4$ and $\theta = 1500$.

correctly reproducing the shape of the experimental pressure profiles, and in particular, the rapid rise in the measured pressure towards the end of the compression. In fact, we shall see below that the algorithm accurately reproduces the experimental compression behaviour in detail. Within the context of the model presented here, the rapid pressure rise is easily explained; near the end of compression, the wave, which carries with it an increase in pressure, passes through a particular point in the chamber with much increased frequency (principally) because the distance it has to travel to return to that point has reduced by a factor of $O(10)$.

Table 2. Comparison of results generated by the algorithm with the numerical results displayed in Figures 3–5. In the table, the first element of a pair (α, β) gives the algorithm value, while the second element gives the corresponding numerical value.

	$[\rho]$	$[T]$	$[p]$
Figure 3	(0.241,0.252)	(0.220,0.222)	(0.514,0.522)
Figure 4	(0.270,0.271)	(0.241,0.250)	(0.694,0.732)
Figure 5	(0.300,0.317)	(0.263,0.262)	(0.913,0.941)

3.4.2. Comparison of algorithm with full numerics

We now give a comparison of the numerical results displayed in Figures 3–5 with the corresponding results generated by the algorithm (34). We denote by $[\rho]$, $[T]$ and $[p]$, the jumps in density, temperature and pressure, respectively, across the shock-front. In Table 2, we compare the values for $[\rho]$, $[T]$ and $[p]$, generated by the algorithm, with those that were obtained by numerically integrating the full equations. Because $\gamma(T) \equiv \gamma_0$ (a constant) in the numerical results, we can use the exact expressions (31) and (33) for \dot{q}_{N0}^+ and \dot{q}_{N0}^- , respectively. The correspondence between the two sets of results is good; the difference that there is in the results is due primarily to the fact that the algorithm is based on a leading order asymptotic analysis. There will also be some error in the numerical results.

3.4.3. The continuum limit as $\theta \rightarrow \infty$

We now consider the continuum limit of the discrete algorithm (34) for $\theta \gg 1$. This corresponds to considering the behaviour for a large number of reflections since the speed of sound in the gas is proportional to $\sqrt{\theta}$ for $\theta \gg 1$.

As $\theta \rightarrow \infty$, it is readily shown from (34) that

$$\begin{aligned}
 \dot{q}_N^+ &\sim \sqrt{\gamma(T_{2N-2})T_{2N-2}\theta}, \quad \dot{q}_N^- \sim -\dot{q}_N^+, \\
 t_{2N} - t_{2N-2} &\sim \frac{2}{\dot{q}_N^+}(1 - t_{2N-2}), \\
 p_{2N} - p_{2N-2} &\sim \frac{2\dot{q}_N^+}{\theta}\rho_{2N-2}, \\
 \rho_{2N} - \rho_{2N-2} &\sim \frac{2}{\dot{q}_N^+}\rho_{2N-2}.
 \end{aligned} \tag{35}$$

We write $t = t_{2N-2}$, $p(t) = p_{2N-2}$, $\rho(t) = \rho_{2N-2}$, $T(t) = T_{2N-2}$, and

$$\frac{dZ(t)}{dt} = \lim_{\theta \rightarrow \infty} \left\{ \frac{Z_{2N} - Z_{2N-2}}{t_{2N} - t_{2N-2}} \right\},$$

where $Z = p, \rho$. Equations (35) then imply that

$$\begin{aligned}\frac{d\rho(t)}{dt} &= \frac{\rho(t)}{1-t}, \\ \frac{dp(t)}{dt} &= \frac{\gamma(T(t))p(t)}{1-t}, \\ p(t) &= \rho(t)T(t), \quad \gamma(T) = \gamma_0 + \gamma_1 T,\end{aligned}\tag{36}$$

$$p(0) = \rho(0) = T(0) = 1,$$

and integration of these equations gives

$$p(t) = \frac{1 - \gamma_0}{\gamma_1(1-t) + (1 - \gamma_0 - \gamma_1)(1-t)^{\gamma_0}}, \quad \rho(t) = \frac{1}{1-t},$$

$$T(t) = \frac{1 - \gamma_0}{\gamma_1 + (1 - \gamma_0 - \gamma_1)(1-t)^{\gamma_0-1}}.$$

For $\gamma \equiv \gamma_0$, these expressions reduce to

$$\rho(t) = \frac{1}{(1-t)^{\gamma_0}}, \quad \rho(t) = \frac{1}{1-t}, \quad T(t) = \frac{1}{(1-t)^{\gamma_0-1}},$$

and these simple results are consistent with the curves displayed in Figure 6(a). The expression for $\rho(t)$ states that the gas density is inversely proportional to the volume of the chamber.

It follows easily from (36) that

$$\frac{dp}{p} = \frac{\gamma(T)}{(\gamma(T) - 1)} \frac{dT}{T},$$

which is the isentropic relation (1) referred to in the introduction.

3.4.4. Variable piston velocity

Obviously, during any compression, there are periods when the pistons are accelerating and decelerating, and it is not difficult to incorporate variable piston motion, $x = X_p(t)$, into the algorithm. The background analysis is almost identical to that of the constant piston velocity case, and we shall confine ourselves to quoting the results here. We now have

$$p_0 = \rho_0 = T_0 = 1, \quad t_0 = 0,$$

with for $N = 1, 2, 3, \dots$,

$$\begin{aligned}\dot{q}_N^+ &= \sqrt{\gamma(T_{2N-2})T_{2N-2}\theta}, & \rho_{2N-1} &= \frac{\dot{q}_N^+}{\dot{q}_N^+ - \dot{X}_p(t_{2N-2})} \rho_{2N-2}, \\ p_{2N-1} &= p_{2N-2} + \frac{\dot{q}_N^+ \dot{X}_p(t_{2N-2})}{\theta} \rho_{2N-2}, & T_{2N-1} &= \frac{p_{2N-1}}{\rho_{2N-1}}, \\ t_{2N-1} &= t_{2N-2} + \frac{1 - X_p(t_{2N-2})}{\dot{q}_N^+}, & \dot{q}_N^- &= -\sqrt{\gamma(T_{2N-1})T_{2N-1}\theta}, \\ \rho_{2N} &= \frac{\dot{q}_N^- - \dot{X}_p(t_{2N-1})}{\dot{q}_N^-} \rho_{2N-1}, & p_{2N} &= p_{2N-1} - \frac{\dot{q}_N^- \dot{X}_p(t_{2N-1})}{\theta} \rho_{2N}, \\ T_{2N} &= \frac{p_{2N}}{\rho_{2N}}, & t_{2N} &= t_{2N-1} + \frac{1 - X_p(t_{2N-1})}{\dot{X}_p(t_{2N-1}) - \dot{q}_N^-}.\end{aligned}\tag{37}$$

It is clear that this algorithm reduces to the correct forms for the particular cases $\dot{X}_p(t) = 1$ and $\dot{X}_p(t) = 0$.

In Figure 6(b), we have plotted a solution calculated using the scheme (37) with

$$X_p(t) = \begin{cases} 1.25t^2 & \text{for } 0 \leq t < 0.4, \\ t - 0.2 & \text{for } 0.4 \leq t < 1, \\ 0.8 + (t - 1) - 2.5(t - 1)^2 & \text{for } 1 \leq t < 1.2, \\ 0.9 & \text{for } t \geq 1.2, \end{cases} \quad (38)$$

which corresponds to uniform acceleration from rest and uniform deceleration to rest at the beginning and end of the piston motion, respectively. When the pistons stop, the algorithm predicts that the pressure, temperature and density in the chamber core remain at the values attained at the end of the compression. Within the context of the model presented in this paper, the calculation of changes in (p, ρ, T) in the core post-compression requires the consideration of higher-order terms in the asymptotic expansions. However, chemical effects are frequently significant post-compression, so that the model analyzed here may not be valid after the pistons have drawn to a stop; we shall return to this issue in more detail in Section 4.

3.5. COMPARISON WITH EXPERIMENTAL DATA

In Figure 7 we give some comparisons between experimental results and the predictions of the model. The experimental data is taken from Musch [16], and each of the three experimental curves has an initial temperature of 295 K and an initial pressure of 0.06 MPa. The results are displayed in non-dimensional form.

An approximation for $X_p(t)$ was obtained using measurements for the piston motion. For the machine at NUI, Galway, the pistons spend about 30% of the compression time accelerating from rest, less than 15% of the time decelerating to rest, and the remainder of the time at a constant maximum velocity of about 14 ms^{-1} . It is found that the first phase of the motion can be reasonably well described by assuming that the pistons are accelerating uniformly. However, the final phase of the motion does not conform to uniform deceleration since measurements indicate that there is a slight rebound in the pistons at the end of their stroke. This rebound increases the final volume of the compression chamber slightly, causing a slight drop in the pressure; this accounts for the kink in the peak of the model pressure profiles in Figure 7, an effect which is also clearly visible in the experimental profiles.

Piston crevices were used in the generation of the experimental data illustrated in Figure 7, and care must be taken to account for the volume which the crevices add to the chamber volume when modelling the behaviour. For the results displayed here, the crevices increase the initial volume of the chamber by about 1.5%. The parameter values used to generate the model curves of Figure 7 are given in Table 3; these parameters were calculated using the data for the experimental conditions and known data for the gases ([9]).

It is clear from Figure 7 that the correspondence between theoretical prediction and experimental result is excellent in all three cases for almost all of the compression time. For Nitrogen and Oxygen, the model also captures the behaviour very well towards the end of the compression, and post-compression. However, for Argon, the model significantly over-predicts the final pressure in the chamber core, and this highlights a weakness of the algorithm. The algorithm predicts that, when the pistons stop, the temperature and pressure in the core remain at the values attained at the end of compression, since this is what the leading-order

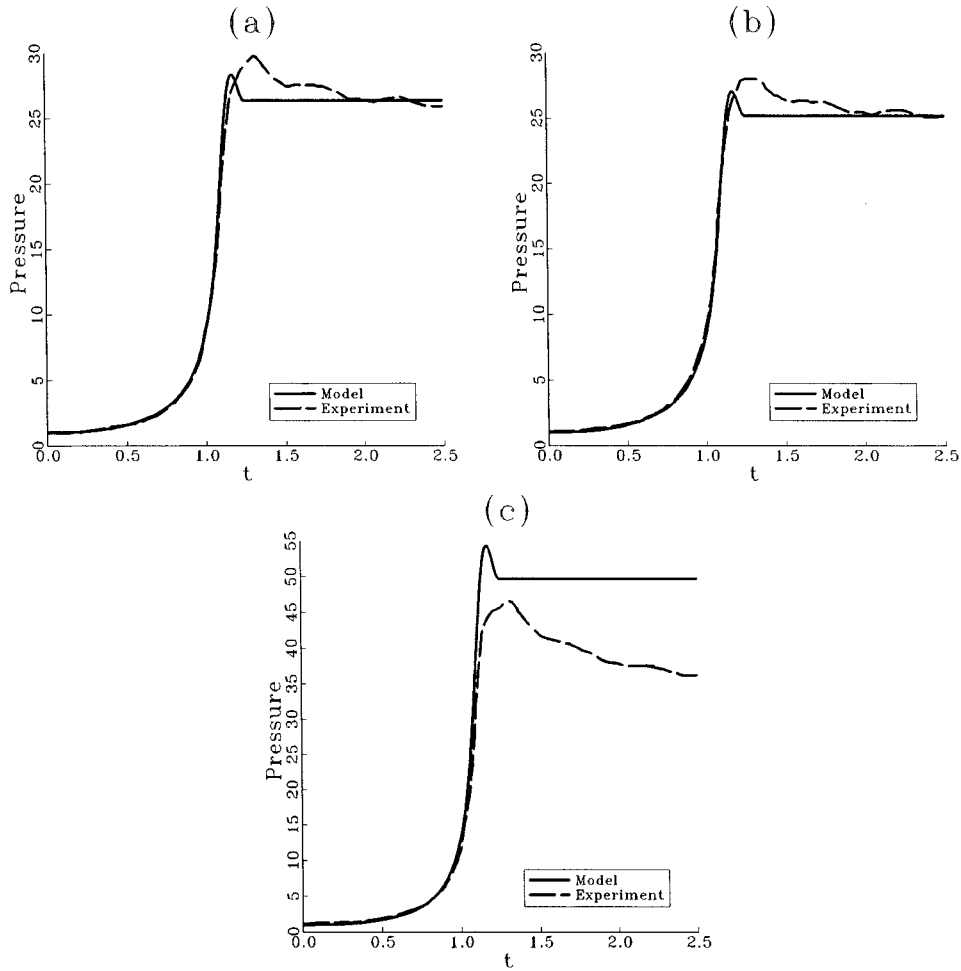


Figure 7. Comparison of model predictions with experimental data taken from [16] for (a) Nitrogen, (b) Oxygen and (c) Argon. The parameter values used in the model are given in Table 3, Section 3.5.

Table 3. Parameter values used to generate the model curves in Figure 7.

Figure	Gas	θ	$\gamma(T)$
7(a)	Nitrogen (N_2)	495	$1.43 - 0.03T$
7(b)	Oxygen (O_2)	395	$1.42 - 0.03T$
7(c)	Argon (Ar)	316	1.67

asymptotic analysis of the governing equations predicts. However, heat in the chamber core is continually being lost to the cold walls, and while this is not a leading-order effect in the chamber core, it can nevertheless have a significant effect on the peak pressure for gases, such as Argon, which have relatively large values for $\gamma(T)$. The algorithm is limited by the fact that it is based on a leading order asymptotic analysis, while higher-order effects can sometimes be significant.

4. Discussion

It should be emphasized that we have only modelled the compression phase of the operation of a rapid-compression machine in this paper. The nature of the post-compression problem is typically very different. The principal purpose of a rapid-compression machine is to very quickly push the enclosed gas mixture into a pressure and temperature regime where auto-ignition can occur. An obvious first attempt to model the post-compression behaviour is to assume that the gas very rapidly comes to rest after the pistons stop; the model studied in this paper predicts that the gas motion settles to rest (to a good approximation) over a time period which is $O(1/\sqrt{\theta}) \ll 1$ after the pistons draw to a halt. After compression, one would then use a system of ordinary differential equations to model the concentrations of the reacting chemical species and the temperature in the chamber core. This model would not be valid close to the walls of the chamber as the thermal boundary layer persists and grows after the pistons stop.

For systems where this approach does prove to be an adequate representation of the behaviour, the problem will have split neatly into two distinct parts which can be studied separately. In the first part, the compression (studied here), gas motion dominates and chemical effects are negligible since the pressures and temperatures are low for all but the final few milliseconds of the compression. For the second part, the post-compression behaviour, gas motion is negligible and chemical effects dominate, and we have a system of ordinary differential equations governing the concentrations of the reacting chemical species and the temperature, the initial conditions for which are provided by the state of the system at the end of the compression. However, for systems where there is significant coupling between gas motion and chemical effects after compression, this approach fails. For such systems, the analysis is more difficult because each species in the mixture then has its own partial differential equation governing the evolution of its mass fraction, see [7].

Acknowledgments

We are grateful for funding received from the Higher Education Authority of Ireland under its PRTL program. We would like to thank P. Musch for his help with the experimental data. Finally, we would like to thank the referees for their helpful suggestions.

References

1. W.S. Affleck and A. Thomas, An opposed piston rapid compression machine for preflame reaction studies. *Proc. Inst. Mech. Engrs.* 183 (1969) 365–385.
2. P. Park, Rapid compression machine measurements of ignition delays for primary reference fuels. Ph.D. thesis, M.I.T. (1990).
3. J.F. Griffiths and J.A. Barnard, *Flame and Combustion*. London: Blackie academic and professional (1995) 328pp.
4. L. Brett, J. MacNamara, P. Musch and J.M. Simmie, Simulation of methane autoignition in a rapid compression machine with creviced pistons. *Combust. Flame.* 124 (2001) 326–329.
5. R.J. Tabaczynski, D.P. Hoult and J.C. Keck, High Reynolds number flow in a moving corner. *J. Fluid Mech.* 42 (1970) 249–255.
6. D. Lee, Autoignition measurements and modeling in a rapid compression machine. Ph.D. thesis, M.I.T. (1997).
7. F.A. Williams, *Combustion Theory*. Massachusetts: Perseus Books (1985) 680pp.
8. J.D. Buckmaster(editor), *The Mathematics of Combustion* (2nd ed.). New York: SIAM (1985) 254pp.

9. I. Barin, *Thermochemical Data of Pure Substances, Parts I and II*. Weinheim: John Wiley and sons (1993) 1739pp.
10. J.O. Hirschfelder, C.F. Curtiss and R.B. Bird, *Molecular Theory of Gases and Liquids*. New York: John Wiley (1963) 1249pp.
11. E.A. John, *Gas Dynamics* (2nd ed.). Boston: Allyn & Bacon (1984) 426pp.
12. L.D. Landau and E.M. Lifshitz, *Fluid Mechanics* (2nd ed.). Oxford: Butterworth-Heinemann (1987) 539pp.
13. C.J. Chapman, *High Speed Flow*. Cambridge: Cambridge University Press (2000) 258pp.
14. R.E. O' Malley, *Singular Perturbation Methods for Ordinary Differential Equations*. New York: Springer-Verlag (1991) 225pp.
15. M.H. Holmes, *Introduction to Perturbation Methods*. New York: Springer-Verlag (1995) 337pp.
16. P. Musch, Hydrogen and methane oxidation in an opposed-piston rapid compression machine; computer simulation and model verification. Report CCW99, NUI, Galway (1999).